Article

Colloidal Synthesis of MoSe$_2$/WSe$_2$ Heterostructure Nanoflowers via Two-Step Growth

Yunjeong Hwang [1,2,3] and Naechul Shin [1,2,4,*]

1   Program in Biomedical Science and Engineering, Inha University, Incheon 22212, Korea; ruflus16@kims.re.kr
2   Program in Smart Digital Engineering, Inha University, Incheon 22212, Korea
3   Materials Center for Energy Convergence, Korea Institute of Materials Science (KIMS), 797 Changwondaero, Sungsan-gu, Changwon 51508, Korea
4   Department of Chemical Engineering, Inha University, Incheon 22212, Korea
*   Correspondence: nshin@inha.ac.kr

Abstract: The ability to control the active edge sites of transition metal dichalcogenides (TMDs) is crucial for modulating their chemical activity for various electrochemical applications, including hydrogen evolution reactions. In this study, we demonstrate a colloidal synthetic method to prepare core-shell-like heterostructures composed of MoSe$_2$ and WSe$_2$ via a two-step sequential growth. By overgrowing WSe$_2$ on the surface of preexisting MoSe$_2$ nanosheet edges, MoSe$_2$-core/WSe$_2$-shell heterostructures were successfully obtained. Systematic comparisons of the secondary growth time and sequential order of growth suggest that the low synthetic temperature conditions allow the stable overgrowth of shells rich in WSe$_2$ on top of the core of MoSe$_2$ with low Gibbs formation energy. The electrochemical analysis confirms that the catalytic activity correlates to the core-shell composition variation. Our results propose a new strategy to control the edge site activity of TMD materials prepared by colloidal synthesis, which is applicable to diverse electrochemical applications.

Keywords: transition metal dichalcogenides; MoSe$_2$; WSe$_2$; heterostructure; core-shell; colloidal synthesis

1. Introduction

Transition metal dichalcogenides (TMDs) have attracted tremendous attention owing to their interesting properties originating from their two-dimensional (2D) structures, which generally consist of a central transition metal layer sandwiched between chalcogen atomic layers. Along with the geometry, a diverse selection of constituents (metals and chalcogens), crystal phases (e.g., trigonal prismatic and octahedral), and a number of layers impart characteristic physical properties, depending on the TMD structures. As an example, group VI TMDs, including MoS$_2$ or WSe$_2$, primarily show semiconducting properties with a bandgap of -1 eV, while group V TMDs, such as the semimetallic VSe$_2$ or NbS$_2$ exhibit superconductivity [1,2]. The phase transition between metallic 1T and semiconducting 2H-phases occurs via chemical intercalation [3,4] or laser excitation [5], without changing the TMD layer constituents. Moreover, the optical bandgap of semiconducting TMD layers exhibits a direct-to-indirect transition depending on the number of layers.

More importantly, the dangling bond-free van der Waals (vdW) interactions, together with the analogous crystal structures, allow the preparation of TMD heterostructures with diverse compositions and geometries. The formation of alloyed TMDs with entire solid solution ranges has been demonstrated via tunable bandgap engineering [6,7]. Furthermore, vertically stacked and laterally extended heterostructures with variable optical/electronic properties have been reported [8,9]. Accordingly, numerous preparation techniques, including mechanical exfoliation or physical/chemical vapor deposition, have been employed to prepare TMD-based heterostructures [10–13].

While these methods lead to complex heterostructures with a high level of control from atomically sharp junctions to alloys with arbitrary compositions, their applications are

limited by complicated preparation procedures and low scalability. Alternatively, solution-based synthetic approaches overcome these limitations with scalable growth protocols at relatively mild temperatures [14,15]. Furthermore, a homogenous reaction environment enables the formation of TMD nanosheets with radially outward oriented edges, which is advantageous for catalysis. Regarding the heterostructure formation, TMD catalytic performance is enhanced by preparing type II heterojunctions, because the electron-hole separation facilitates the charge transfer [16–18]. Nevertheless, growing core-shell like TMD heterostructures in the solution phase remains challenging because the thermodynamic control of stepwise nucleation is hindered in the homogeneous precursor mixture.

Here, we present a synthetic approach for the preparation of core-shell-like TMD nanoflower heterostructures based on colloidal crystal growth in the solution phase. We selected $MoSe_2$ and WSe_2 as model systems for the heterostructures because of their comparable lattice constants (2.7 Å for $MoSe_2$ (100) and 2.8 Å for WSe_2 (100)). The sequential colloidal growth using primarily grown $MoSe_2$ nanosheets as the host material for the subsequent nucleation and growth of WSe_2 resulted in the formation of phase-segregated, core-shell-like nanosheets. The systematic comparison of the heterostructure compositional distribution as a function of secondary growth time and growth order provides important information on the thermodynamic and kinetic factors dominating the growth. Specifically, low-temperature conditions and the Gibbs formation energy difference between $MoSe_2$ and WSe_2 enable the stable growth of $MoSe_2$-core/WSe_2-shell heterostructure nanosheets. Moreover, electrochemical measurements based on the hydrogen evolution reaction evaluate the catalytic activity correlation to the core-shell composition. These results suggest that tuning the active site density of colloidally synthesized TMD materials is a crucial strategy for various electrochemical applications.

2. Materials and Methods

2.1. Materials

Molybdenum hexacarbonyl ($Mo(CO)_6$, 98%), tungsten hexacarbonyl ($W(CO)_6$, 99.99 %), tetradecylphosphonic acid (TDPA, 97%), oleic acid (OA, technical, 90%), and diphenyl diselenide (Ph_2Se_2, 98%) were purchased from Sigma-Aldrich (Darmstadt, Germany). Solvents, including toluene (99.5%) and *n*-butanol (99%), were purchased from Duksan (Ansan, South Korea). All chemicals were used as received, without further purification.

2.2. Synthesis of MoSe$_2$, WSe$_2$, and MoSe$_2$/WSe$_2$ Heterostructures

$MoSe_2$ and WSe_2 nanosheets were grown using a colloidal hot-injection method. 108 mg (0.4 mmol) of $Mo(CO)_6$ or 141 mg (0.4 mmol) of $W(CO)_6$ were added into a 100 mL three-neck flask which was pre-loaded with 78.5 mg (0.28 mmol) of TDPA dissolved into 6 g of OA. 250 mg Ph_2Se_2, the selenium precursor, was dissolved in 4 g of OA in a separate vial. The Mo or W precursor mixtures were heated to 130 °C for 10 min and kept for 20 min under Ar atmosphere. The temperature was increased to 350 °C (for $MoSe_2$) and 330 °C (for WSe_2) at a rate of 4 °C/min, followed by the Se precursor solution injection. The nanosheet growth was maintained for 2 h, and then the flask was removed from the heating mantle to gradually cool down to room temperature. The crude solution was diluted with a solvent mixture composed of toluene and *n*-butanol in a 2:1 volume ratio. The suspension was then centrifuged for 30 min at 4000 rpm. The black powdery product was washed three times with a solvent mixture of toluene and *n*-butanol. Core–shell heterostructures were prepared by sequential growth of WSe_2 on $MoSe_2$ nanosheets or vice versa. The as-synthesized $MoSe_2$ and WSe_2 nanosheets were loaded into a 100 mL three-neck flask with 0.4 mmol of $W(CO)_6$ and $Mo(CO)_6$, respectively, and 78.5 mg of TDPA dissolved in 6 g of OA. The temperature profiles and the injection amount of the Se precursor were identical to those of the individual nanosheet growth, except that the secondary growth time varied from 30 min to 6 h.

2.3. Characterization

The as-grown nanosheets dispersed in toluene were drop-casted onto Si and SiO_2/Si substrates, and their morphologies were examined using a scanning electron microscope (SEM, SU8010, Hitachi, Tokyo, Japan). The same substrates were used for the investigation of structures using a custom-built Raman spectrometer equipped with a charge-coupled device (DV420A-OE, Toshiba, Tokyo, Japan). The wavelength and power of the laser were 532 nm and 5 mW, respectively. The sample suspension was drop-cast onto a TEM grid (#01824, Ted Pella, Redding, CA, USA) for transmission electron microscopy (TEM, JEM2100F, JEOL, Tokyo, Japan). Microscopic images and selected area diffraction patterns were obtained under an operating voltage of 200 kV. The crystallinity and chemical composition of the samples were measured using powder X-ray diffraction (PXRD, X'Pert-PRO MRD, PANalytical, Malvern, United Kingdom) and X-ray photoelectron spectroscopy (XPS, K-Alpha, Thermo Scientific, Seoul Korea). Prior to the measurements, the samples were dried at 300 °C for 2 h under N_2 atmosphere.

2.4. Electrochemical Measurements

The hydrogen evolution reaction (HER) was performed with a three-electrode-configuration HER potentiostat (PGSTAT 302N, Autolab, Utrecht, The Netherlands). Graphite rod and KCl-saturated Ag/AgCl were used as the counter and reference electrodes, respectively. The catalyst ink was prepared by mixing 4 mg of the catalyst (sample powders after drying), 30 μL of Nafion solution, and 1 mL of an ethanol-deionized water mixture (1:4 ratio). The mixed ink solution was ultrasonicated for 1 h. The catalyst ink (5 μL) was deposited onto a polished glassy carbon electrode and dried overnight. Linear sweep voltammetry measurements were conducted in 0.5 M H_2SO_4 solution with a sweep rate of 5 mV/s from 0.42 V to −0.78 V vs. reversible hydrogen electrode (RHE).

3. Results and Discussion

The $MoSe_2$/WSe_2 heterostructures were prepared via a sequential two-step colloidal synthesis, as illustrated in Scheme 1. First, $MoSe_2$ nanosheets were primarily grown upon hot injection of diphenyl diselenide dissolved in oleylamine (OA) into a solution of $Mo(CO)_6$ dissolved in OA with TDPA at 350 °C and reacted for 2 h. The as-grown $MoSe_2$ nanosheets served as the substrate for the secondary growth of WSe_2; therefore, $MoSe_2$, $W(CO)_6$, and TDPA were mixed in a three-neck flask, followed by a hot injection of diphenyl diselenide at 350 °C. After 2–6 h growth, the final $MoSe_2$/WSe_2 heterostructures were obtained.
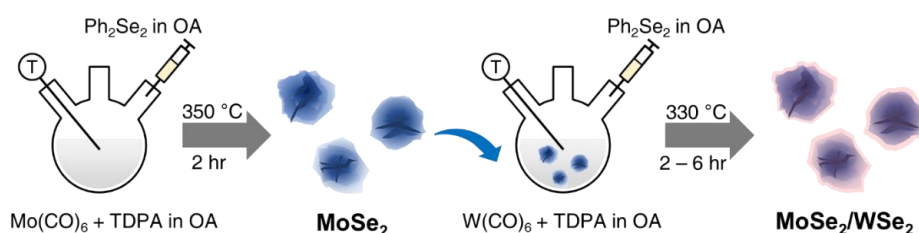
Scheme 1. Schematic illustration of the synthetic process of $MoSe_2$/WSe_2 heterostructure via the two-step colloidal synthesis.

Figure 1a–c illustrates the SEM images of the representative $MoSe_2$, WSe_2, and $MoSe_2$/WSe_2 heterostructures. The agglomerates of nanosheets with flower-like morphologies are confirmed from all the samples, analogously to previous studies [15,19]. The average diameter of the individual domains were in the range 200–300 nm. The powder XRD analysis shown in Figure 1d–f confirmed the correspondence of the agglomerated nanosheet diffraction pattern to the reference data (JCPDS #: 03-065-3999 ($MoSe_2$), 01-089-5257(WSe_2)). Five peaks located at 2θ = 13.6° (or 13.7°), 31.4°, 37.8° (or 37.9°), 47.4°, and 55.9° (or 56.0°) were assigned to the (002), (100), (103), (105), and (110) planes of

MoSe$_2$ (WSe$_2$), respectively, indicating that the as-grown materials displayed the characteristic crystal structures of the 2D TMDs prepared via colloidal synthesis. Notably, since MoSe$_2$ and WSe$_2$ are characterized by comparable crystal structures (2H phase) and lattice constants [15,20], the as-obtained MoSe$_2$/WSe$_2$ hetero-nanosheets exhibited analogous morphologies and XRD peak patterns to the corresponding single TMD counterparts (Figure 1f). Despite the indistinguishable shapes and structures, XPS measurements of the MoSe$_2$/WSe$_2$ hetero-nanosheets (Figure 1g–i) confirmed the concurrent presence of both Mo and W. The peaks located at 229 and 232 eV (Figure 1g) corresponding to 2H MoSe$_2$ (Mo^{4+} 3d$_{5/2}$ and Mo^{4+} 3d$_{3/2}$, respectively) suggested that Mo in the core region of the heterostructure largely retained its unoxidized state [21]. Conversely, the core-level W 4f spectrum of the same sample (Figure 1h) indicated the presence of both oxidized (WO$_3$, W^{6+} 4f$_{5/2}$ at 38 eV and W^{6+} 4f$_{7/2}$ at 36 eV) and unoxidized (2H-WSe$_2$, W^{4+} 4f$_{5/2}$ at 35 eV and W^{4+} 4f$_{7/2}$ at 33 eV) states [22]. The core-level Se^{2-} spectrum (Se^{2-} 3d$_{5/2}$ at 54.5 eV and Se^{2-} 3d$_{3/2}$ at 55.3 eV) shows no direct evidence of Se oxidation, as shown in Figure 1i [23]. The observed distinct oxidized states between Mo and W suggest a selective oxidation of the outer regions, rich in WSe$_2$, whereas the inner domains, primarily consisting of MoSe$_2$, were preserved. Therefore, the results presented in Figure 1 provide initial evidence of the uneven distribution of Mo and W in the MoSe$_2$/WSe$_2$ heterostructures.
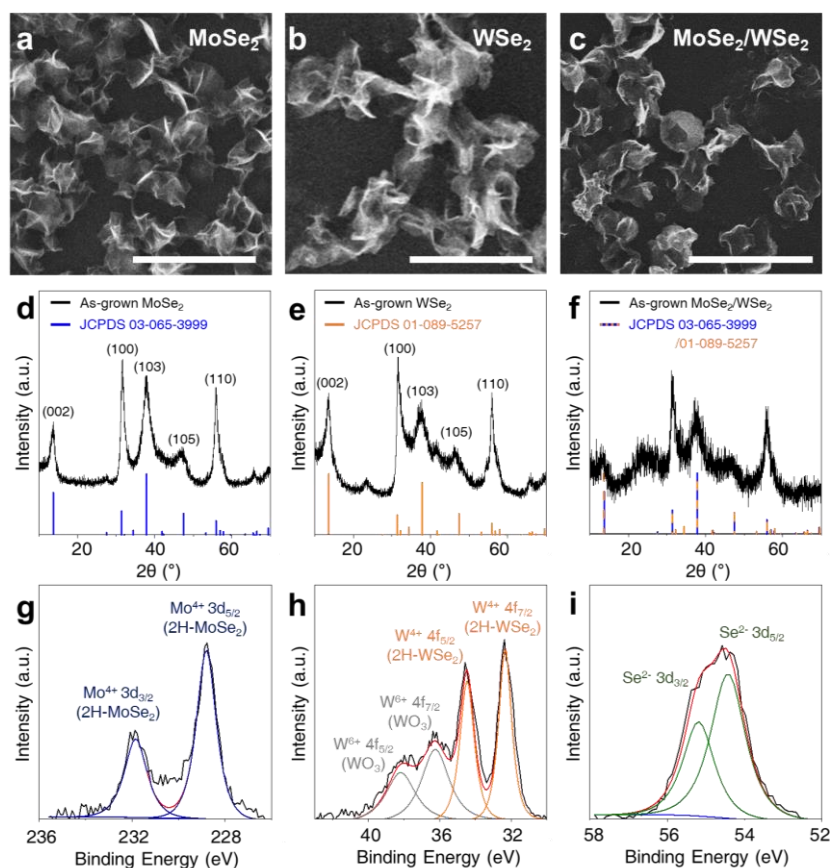

Figure 1. SEM images of the colloidally synthesized (**a**) MoSe$_2$, (**b**) WSe$_2$, and (**c**) MoSe$_2$/WSe$_2$ hetero-nanosheets. Scale bars, 1 μm. Powder XRD spectra obtained from (**d**) MoSe$_2$, (**e**) WSe$_2$, and (**f**) MoSe$_2$/WSe$_2$ nanosheets, shown together with the reference peaks from the corresponding JCPDS library (MoSe$_2$: JCPDS 03-065-3999 and WSe$_2$: JCPDS 01-089-5257). Core-level XPS spectra of (**g**) Mo 3d, (**h**) W 4f, and (**i**) Se 3d of MoSe$_2$/WSe$_2$ hetero-nanosheets.

TEM measurements were conducted to investigate the as-grown-nanosheet crystal structure. Figure 2a–c display low-magnification TEM images of individual MoSe$_2$, WSe$_2$, and MoSe$_2$/WSe$_2$ nanosheets, respectively, confirming their nanoflower-like morphologies with noticeable thin edges. High-resolution TEM (HRTEM) images obtained near the edges

of each sample (highlighted by dashed red boxes) are shown in Figure 2d–f. Lattice fringes spaced by 2.7 Å (Figure 2d) and 2.8 Å (Figure 2e), corresponding to the (100) planes of $MoSe_2$ and WSe_2, showed six-fold symmetry [15,20]. The selected area electron diffraction (SAED) patterns in the insets exhibited clear diffraction spot separation with the zone axis along the [001] direction, confirming that the edges of both $MoSe_2$ and WSe_2 are primarily composed of highly crystalline monolayers. While similar six-fold symmetric lattice fringes were observed for the $MoSe_2/WSe_2$ heterostructures, the fast Fourier transform (FFT) pattern (inset of Figure 2f) was stretched along the edges, reflecting the presence of curved monolayers facing outwards.
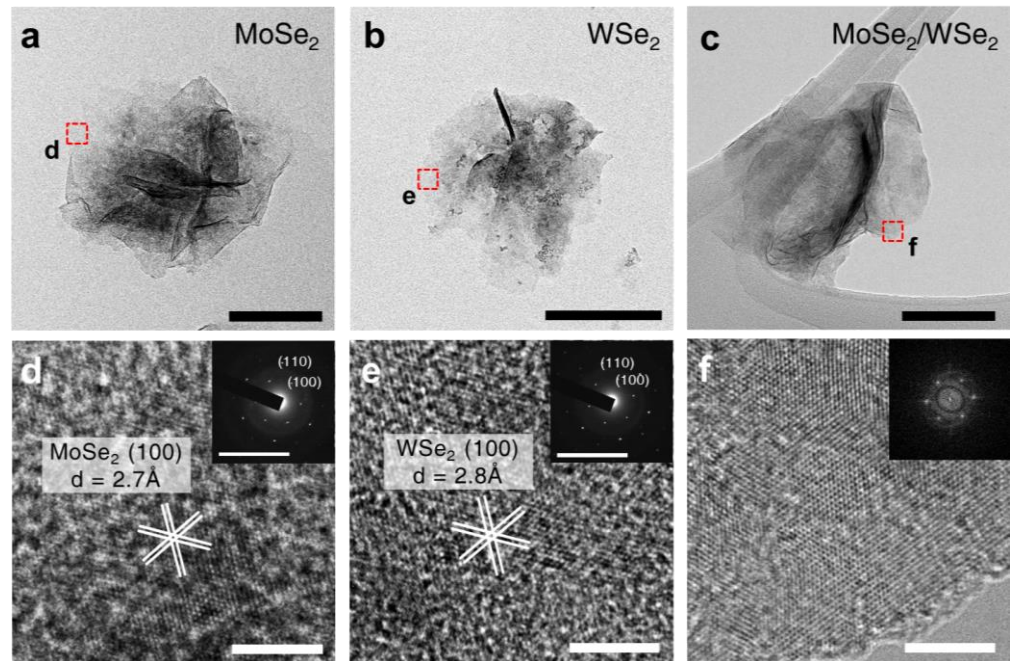

Figure 2. (**a**–**c**) Low-magnification bright field TEM images of (**a**) $MoSe_2$, (**b**) WSe_2, and (**c**) $MoSe_2/WSe_2$ hetero-nanosheets. Scale bars: (**a**,**b**) 200 nm and (**c**) 300 nm. (**d**–**f**) HRTEM images corresponding to the regions highlighted by dashed red boxes shown in (**a**–**c**) Scale bars: (**d**,**e**) 5 nm and (**f**) 20 nm. Insets in (**d**–**f**) correspond to the SAED and FFT patterns. Scale bars, $100\ nm^{-1}$.

Figure 3a,b show the energy-dispersive X-ray spectroscopy (EDS) measurements of a representative $MoSe_2/WSe_2$ heterostructure. The elemental mappings of Mo, W, and Se (Figure 3b) confirmed that the spatial distributions of Mo and W are distinct in a 350 nm-sized hetero-nanosheet. While the signals of Mo are prominent only within the core region (200 nm), those of W appear uniformly distributed across all the domains (350 nm). The spatially distinct distributions of Mo and W were further validated by superimposing the mapping images (lower right panel of Figure 3b). Hence, the $MoSe_2/WSe_2$ hetero-nanosheets prepared via the two-step method exhibited core-shell-like structures. As the SEM and TEM images of $MoSe_2$ and WSe_2 in Figures 1 and 2 indicate that the as-grown individual nanosheets exhibit three-dimensionally connected planar edges, we speculate that the sequential growth will result in the formation of WSe_2 secondary layers both on top of the planes and along the edges of $MoSe_2$, as illustrated in Figure 3c.
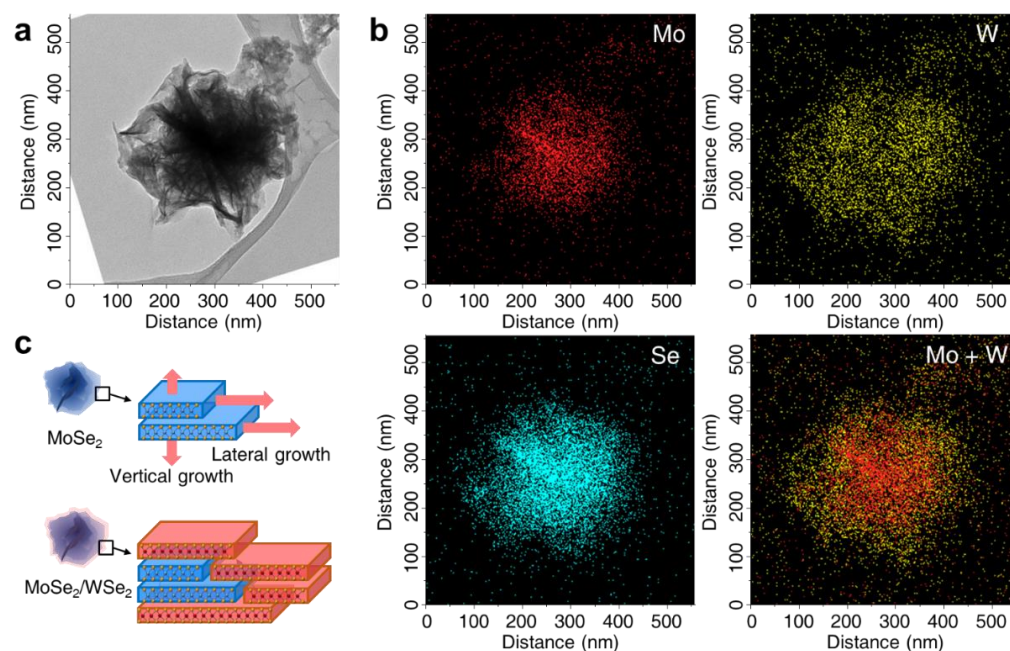
Figure 3. (**a**) Low-magnification TEM image of a MoSe$_2$/WSe$_2$ heterostructure and (**b**) corresponding EDS elemental maps of Mo, W, and Se in the heterostructure. The bottom right panel of (**b**) is a superimposed image of Mo and W spatial distribution. (**c**) Schematic illustration showing the heterostructure formation via vertical and lateral growth of WSe$_2$ layers on the preexisting MoSe$_2$ edge surface.

To corroborate the core-shell-like growth of WSe$_2$ on MoSe$_2$, we systemically investigated the distribution of W in the heterostructures as a function of the secondary growth time. Three samples were prepared by varying the secondary growth times, as shown in the TEM images in Figure 4a. Here, MW22, MW24, and MW26 denote the heterostructures of WSe$_2$ grown for 2, 4, and 6 h, respectively, over the primary MoSe$_2$ nanoflowers obtained after 2 h of growth. The profiles of W:Mo and Se:Mo atomic ratios corresponding to the 11 linear yellow dots crossing each nanoflower are shown in Figure 4b. For comparison, the ratios were normalized to the point with the highest Mo concentration. Notably, W atomic ratio increased in the outer domain region with the secondary growth time, consistently with the core-shell-like growth of WSe$_2$. Figure 4c shows the W:Mo ratio distribution across the nanoflower domains. While the ratio near the outer edges drastically increased with the growth time, near the center it remained lower than 1. The change in the overall W:Mo ratio of each sample (Figure 4d) further corroborated the increase in W concentration proportionally to the secondary growth time. Remarkably, WSe$_2$ layer heterogeneous nucleation was favored on the surface of the pre-grown MoSe$_2$ domains for the core-shell structures observed in this study. The activation energy barrier for WSe$_2$ nucleation on the preexisting MoSe$_2$ surface was lower than that for homogeneous nucleation because of the reduced surface free energy [24]. Since the individual WSe$_2$ nanosheets were absent in the samples grown via this two-step growth, it is speculated that the core-shell-like growth was favored over the independent nucleation, especially considering the maximum growth temperature of colloidal synthesis of 400 °C.

While the formation of the phase-segregated structures was preferred to the mixed alloys under our selected growth conditions, the difference in the formation enthalpy between MoSe$_2$ and WSe$_2$ may affect the spatial distribution of the components (i.e., core vs. shell), according to the chronological order of the growth protocol. Figure 5 displays the results of the heterostructure growth in reverse order for WSe$_2$ growth for 2 h, followed by MoSe$_2$ growth for 30 min (marked as WM2$\frac{1}{2}$). While both TEM and HRTEM images indicate that the nanosheet size and the monolayer edge configurations are similar to

those of the MW samples (Figure 5a,b), the elemental analysis across the domain points out striking differences. The concentration of W was substantially lower than that of Mo, and only a small amount was detected near the edge (Figure 5c), indicating that W in the primary nanosheet structure can dynamically interchange with Mo during the secondary growth.
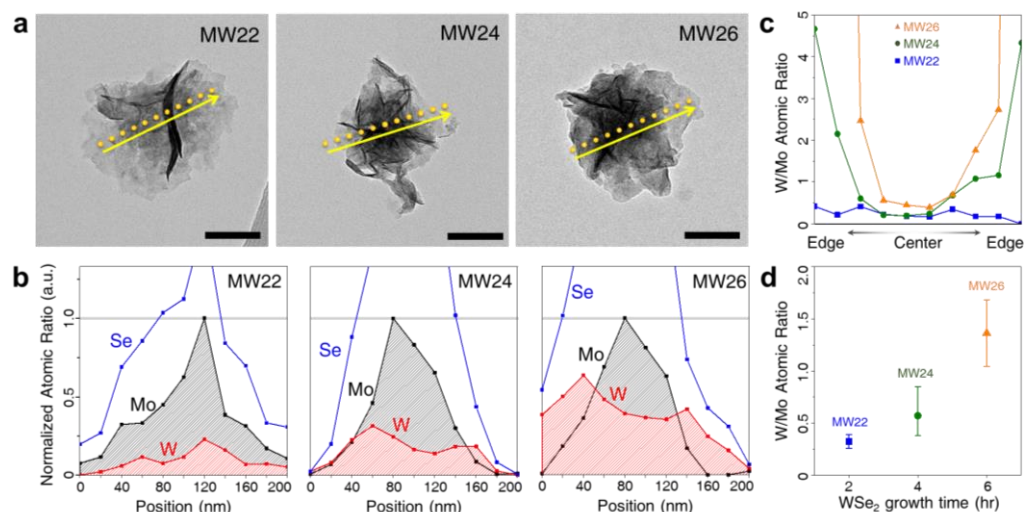

Figure 4. (**a**) TEM images of the $MoSe_2$/WSe_2 heterostructures prepared from different WSe_2 secondary growth times (2, 4, and 6 h) on the primary $MoSe_2$ nanosheets pre-grown for 2 h. Scale bars, 100 nm. (**b**) Corresponding elemental ratios of Mo, W, and Se obtained from the point EDS spectra measured across the nanostructure domains. The point arrays of the measurements are highlighted by the yellow dots in (**a**). All the ratios were normalized to the positions with the highest Mo concentration (highlighted by the horizontal gray lines). (**c**) Profiles of W/Mo atomic ratio according to the relative positions from the domain center. (**d**) W/Mo atomic ratios as a function of the secondary WSe_2 growth time.
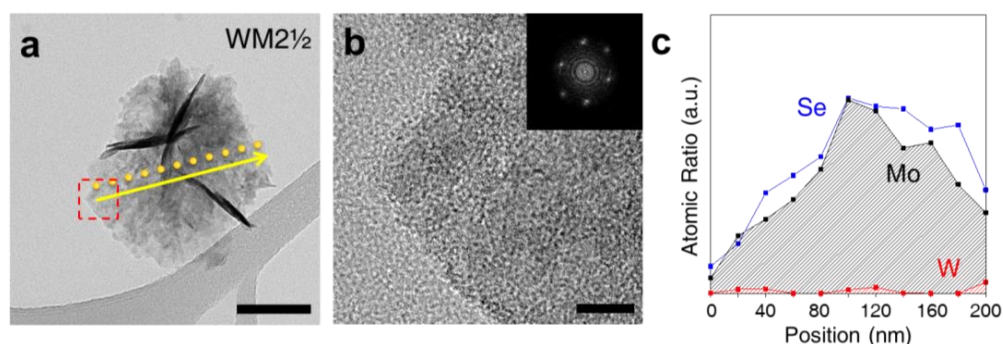

Figure 5. (**a**) Low-magnification TEM image of a nanostructure obtained from 30 min $MoSe_2$ secondary growth on the WSe_2 nanosheets pre-grown for 2 hrs. Scale bar, 100 nm. (**b**) HRTEM image measured at the edge region highlighted by the dashed red box in (**a**). The inset indicates the corresponding FFT pattern. Scale bar, 10 nm. (**c**) Elemental ratio profiles of Mo, W, and Se across the nanostructure, obtained from the point arrays highlighted by the yellow dots in (**a**).

Two possible explanations of the observed Mo-rich nanosheets from the reverse order growth can be considered. First, the $MoSe_2$ nanosheet particles grew homogeneously without the pre-grown WSe_2 surface assistance. According to this assumption, both $MoSe_2$ and WSe_2 independently exist in the final product. However, no WSe_2 nanosheets were observed in this sample, suggesting that the hypothesis of homogeneous nucleation can be excluded. The second suggested scenario considers the substitution via interdiffusion of W in the primarily-grown-WSe_2 nanosheet by Mo during the second step. The lower

Gibbs free energy for the $MoSe_2$ formation compared to WSe_2 under the selected growth temperature (<700 °C) [25] suggests that $MoSe_2$ tends to reduce its surface energy relatively to WSe_2. Thus, Mo diffused towards the nanosheet core upon shell growth on the preexisting WSe_2 nanosheet surfaces. Noticeably, the formation of the $Mo_{1-x}W_xSe_2$ alloy was unlikely because of the low-temperature conditions used in colloidal synthesis, with a consequent reduction of the entropic contribution to the formation energy of mixed alloys. A similar behavior was observed in the two-step sequential growth of the WS_2/MoS_2 heterostructure employing the chemical vapor deposition (CVD) technique, as reported by Bogaert et al. [26]. In that case, the sequential growth of WS_2-MoS_2 showed the formation of $Mo_{0.5}W_{0.5}S_2$ at high temperatures (>680 °C), whereas the MoS_2 core-WS_2 shell heterostructure was found at a low temperature (650 °C), which was reversed from the growth order. Hence, our observations indicate that the compositional distribution of the core-shell heterostructures is dominated by the thermodynamic preferences of their constituents.

Figure 6a shows the Raman spectra of the core-shell heterostructures prepared with various $MoSe_2$ secondary growth times. The Raman peaks of the pure $MoSe_2$ nanosheet (black) are located at 240 and 283 cm^{-1}, corresponding to the out-of-plane A_{1g} and in-plane E^1_{2g} modes, respectively, whereas the WSe_2 nanosheet (red) exhibits a degenerated E^1_{2g}-like peak centered at 249 cm^{-1} [26,27]. While the hetero-nanosheets (MW21, MW22, MW24, and MW26) displayed Raman spectra largely similar to the core-only $MoSe_2$, the emergence of the shoulder peaks at 249 cm^{-1} and their increase in intensity were evident as the secondary growth time increased from 1 h to 6 h. Notably, the $MoSe_2$ peaks of the heterostructures did not exhibit a shift in wavenumbers, suggesting that the WSe_2 shell growth did not affect the lattice strain of the $MoSe_2$ core. Furthermore, the typical features of the A_{1g} blue-shift and E^1_{2g} red-shift corresponding to the formation of $Mo_xW_{1-x}Se_2$ alloy were absent [28], supporting the core-shell-like structure for all the samples. To confirm the compositional dependence of the heterostructures on the secondary growth time, the Raman intensity ratio of the characteristic E^1_{2g} peak of WSe_2 (249 cm^{-1}) to $MoSe_2$ (240 cm^{-1}) was plotted as a function of WSe_2 growth time, as illustrated in Figure 6b. The tendency of the asymptotic increase in the intensity ratio with the secondary growth time confirmed the tunable overgrowth of the WSe_2 shell, which is immiscible with the $MoSe_2$ core.
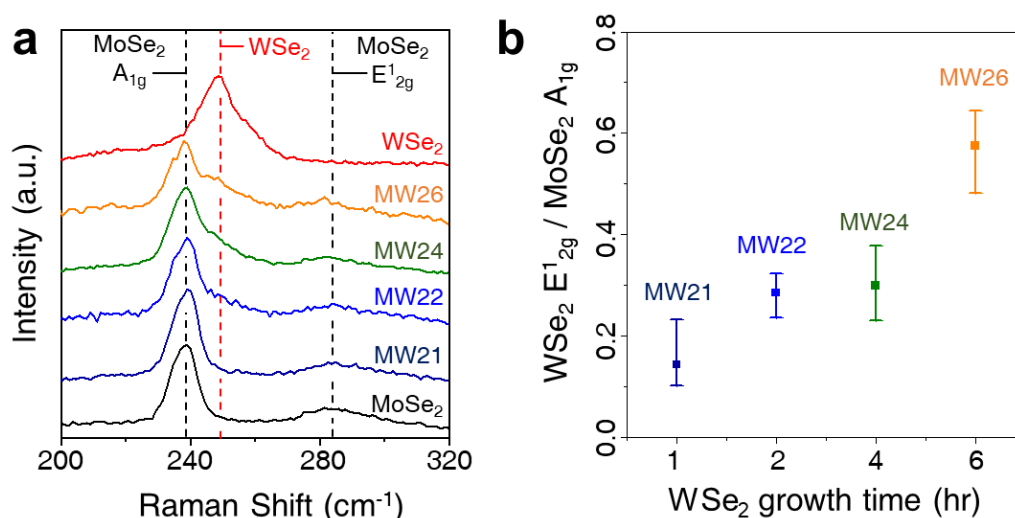

Figure 6. (**a**) Raman spectra of $MoSe_2/WSe_2$ heterostructures (MW21, MW22, MW24, and MW26), shown together with the data of pure $MoSe_2$ and WSe_2. The vertical dashed black lines correspond to the $MoSe_2$ A_{1g} (239 cm^{-1}) and E^1_{2g} (283 cm^{-1}) peaks. The vertical dashed red line denotes the WSe_2 E^1_{2g} (249 cm^{-1}) peak. (**b**) Raman intensity ratio of WSe_2 E^1_{2g} to $MoSe_2$ A_{1g} as a function of the secondary WSe_2 growth time.

The obtained $MoSe_2/WSe_2$ core-shell heterostructures with variable shell thicknesses were further applied to the HER electrochemical reaction. We compared the HER performance of the as-grown heterostructures using a three-electrode configuration, as shown in Figure 7. Figure 7a shows the linear sweep voltammetry (LSV) curves of MW22 and MW24 transferred onto glassy carbon (GC) electrodes. The data from pure $MoSe_2$ and WSe_2 are shown together with the Pt electrode, as a reference. The overpotential values at a current density of 10 mA/cm^2 were 80, 340, 410, 580, and 650 mV for Pt, $MoSe_2$, MW22, MW24, and WSe_2, respectively.
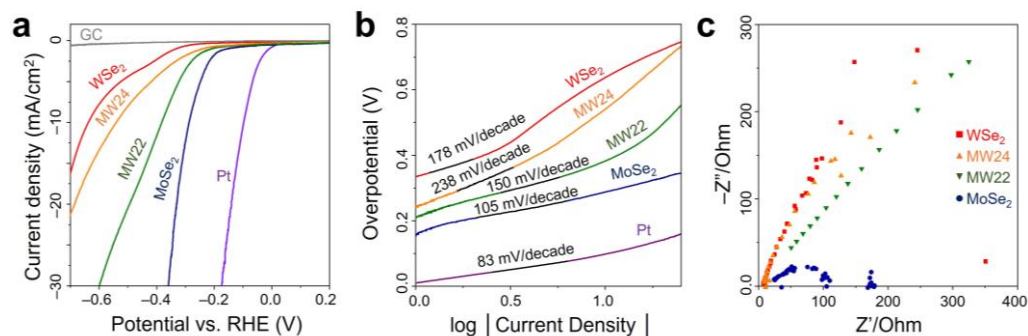

Figure 7. (**a**) Linear sweep voltammetry (LSV) analysis conducted on Pt, $MoSe_2$, MW22, MW24, WSe_2, and GC (glassy carbon) electrodes. (**b**) Tafel slopes corresponding to the LSV analysis shown in (**a**). (**c**) Nyquist plots obtained from the electrochemical impedance spectroscopy (EIS) measurements.

While $MoSe_2$ required a lower overpotential than WSe_2, the heterostructures exhibited intermediate performance according to the WSe_2 shell growth time. The corresponding Tafel slopes (Figure 7b) of 83 (Pt), 105 ($MoSe_2$), 150 (MW22), 238 (MW24), and 178 (WSe_2) mV/decade additionally reflected the relative HER performance. Finally, the Nyquist plot obtained from the electrochemical impedance spectroscopy (EIS) shown in Figure 7c further confirmed that the resistance of MW22 (580 Ω) and MW24 (713 Ω) is between that of $MoSe_2$ (86 Ω) and WSe_2 (1652 Ω). Table 1 summarizes the electrochemical performances of the colloidal TMDs prepared in this study compared with previously reported data. While the absolute performance values are inferior to the published values, presumably owing to the presence of residual precursors, our results provide important implications regarding the dependence of electrochemical activity on structural characteristics of $MoSe_2/WSe_2$ core-shell heterostructures. Given that the edges of $MoSe_2$ exhibit lower hydrogen adsorption energy relative to WSe_2, the increase in the shell growth time would result in the reduction of $MoSe_2$ edges and a subsequent decrease in the electrochemical activity. Thus, the intermediate HER performances of heterostructures, dependent on the secondary growth time, suggest that the core-shell growth protocol proposed in this study can be applied to tune the electrochemical activities of colloidal TMD materials.

Table 1. HER performance comparison of $MoSe_2$-based nanostructure catalysts showing the overpotentials and Tafel slopes.

Materials	Loading	η at j = 10 mA/cm^2 (mV)	Tafel Slope (mV/decade)	Ref.
$MoSe_2$ nanoflowers		340	105	
MW22 nanoflowers	0.28 mg cm^{-2}	410	150	This work
MW24 nanoflowers	on GC	580	238	
WSe_2 nanoflowers		650	178	
Bulk $MoSe_2$	0.28 mg cm^{-2} on GC	>600	346	[14]
Porous $MoSe_2$ nanosheets	0.47 mg cm^{-2} on GC	150	80	[29]

Table 1. *Cont*.

Materials	Loading	η at j = 10 mA/cm^2 (mV)	Tafel Slope (mV/decade)	Ref.
Vertically aligned MoSe$_2$ layers	0.0135 mg cm^{-2} on GC	−450	105–120	[30]
Hierarchical MoSe$_{2-x}$ nanosheets	0.28 mg cm^{-2} on GC	288	98	[14]
MoSe$_2$ nanoflakes (2:1 ratio to Ketjen black)	0.28 mg cm^{-2} on GC	181 ± 1	45 ± 1	[31]
MoSe$_2$ nanonetworks (8:1 ratio to Ketjen black)	0.28 mg cm^{-2} on GC	302	109	[19]
MoSe$_2$ nanoflowers (8:1 ratio to Ketjen black)	0.28 mg cm^{-2} on GC	233	89	[19]

4. Conclusions

We presented core-shell heterostructures of MoSe$_2$/WSe$_2$ TMDs obtained via a two-step colloidal synthesis. Comprehensive structural and chemical analyses confirmed that the as-grown heterostructures were composed of a spatially distinct 2H-MoSe$_2$ core and WSe$_2$ shell layers. Due to the lower regime of synthetic temperatures relative to the vapor-phase-based approach, the colloidal growth of TMDs in solution enables the formation of phase-segregated, core-shell-like structures rather than uniformly distributed alloys. The composition of the shell layer was tunable by changing the secondary growth time, and the spatial distribution of constituents in the heterostructure was thermodynamically determined as such MoSe$_2$ resides in the core region. Notably, the electrochemical properties measured from the as-grown samples correlated to the variety of core-shell compositions. Our results offer an opportunity to control the properties of colloidal TMDs, depending on the edge structure. The ability to modulate electrochemistry by engineering active edge sites is critical for developing highly efficient HER electrocatalysts.

Author Contributions: Conceptualization, N.S.; methodology, Y.H.; validation, Y.H. and N.S.; formal analysis, Y.H.; investigation, Y.H.; resources, N.S.; data curation, Y.H. and N.S.; writing—original draft preparation, Y.H. and N.S.; writing—review and editing, N.S.; visualization, Y.H. and N.S.; supervision, N.S.; project administration, N.S.; funding acquisition, N.S. All authors have read and agreed to the published version of the manuscript.

Institutional Review Board Statement: Not applicable.

Informed Consent Statement: Not applicable.

Data Availability Statement: The data presented in this study are available in this article.

Conflicts of Interest: The authors declare no conflict of interest.

References

1. Choi, W.; Choudhary, N.; Han, G.H.; Park, J.; Akinwande, D.; Lee, Y.H. Recent Development of Two-Dimensional Transition Metal Dichalcogenides and Their Applications. *Mater. Today* **2017**, *20*, 116–130. [CrossRef]
2. Kim, S.Y.; Kwak, J.; Ciobanu, C.V.; Kwon, S.Y. Recent Developments in Controlled Vapor-Phase Growth of 2D Group 6 Transition Metal Dichalcogenides. *Adv. Mater.* **2019**, *31*, 1804939. [CrossRef]
3. Huang, Q.; Li, X.; Sun, M.; Zhang, L.; Song, C.; Zhu, L.; Chen, P.; Xu, Z.; Wang, W.; Bai, X. The Mechanistic Insights into the 2H-1T Phase Transition of MoS$_2$ upon Alkali Metal Intercalation: From the Study of Dynamic Sodiation Processes of MoS$_2$ Nanosheets. *Adv. Mater. Interfaces* **2017**, *4*, 1700171. [CrossRef]

4. Fan, S.; Zou, X.; Du, H.; Gan, L.; Xu, C.; Lv, W.; He, Y.B.; Yang, Q.H.; Kang, F.; Li, J. Theoretical Investigation of the Intercalation Chemistry of Lithium/Sodium Ions in Transition Metal Dichalcogenides. *J. Phys. Chem. C* **2017**, *121*, 13599–13605. [CrossRef]

5. Cho, S.; Kim, S.; Kim, J.H.; Zhao, J.; Seok, J.; Keum, D.H.; Baik, J.; Choe, D.; Chang, K.J.; Suenaga, K.; et al. Phase Patterning for Ohmic Homojunction Contact in MoTe$_2$. *Science* **2015**, *349*, 625–628. [CrossRef]

6. Park, J.; Kim, M.S.; Park, B.; Oh, S.H.; Roy, S.; Kim, J.; Choi, W. Composition-Tunable Synthesis of Large-Scale Mo$_{1-x}$W$_x$S$_2$ Alloys with Enhanced Photoluminescence. *ACS Nano* **2018**, *12*, 6301–6309. [CrossRef]

7. Susarla, S.; Kutana, A.; Hachtel, J.A.; Kochat, V.; Apte, A.; Vajtai, R.; Idrobo, J.C.; Yakobson, B.I.; Tiwary, C.S.; Ajayan, P.M. Quaternary 2D Transition Metal Dichalcogenides (TMDs) with Tunable Bandgap. *Adv. Mater.* **2017**, *29*, 1702457. [CrossRef]

8. Wu, Y.; Xu, M.; Chen, X.; Yang, S.; Wu, H.; Pan, J.; Xiong, X. CTAB-Assisted Synthesis of Novel Ultrathin MoSe$_2$ Nanosheets Perpendicular to Graphene for the Adsorption and Photodegradation of Organic Dyes under Visible Light. *Nanoscale* **2016**, *8*, 440–450. [CrossRef]

9. Jung, Y.; Shen, J.; Liu, Y.; Woods, J.M.; Sun, Y.; Cha, J.J. Metal Seed Layer Thickness-Induced Transition from Vertical to Horizontal Growth of MoS$_2$ and WS$_2$. *Nano Lett.* **2014**, *14*, 6842–6849. [CrossRef] [PubMed]

10. Pezeshki, A.; Shokouh, S.H.H.; Nazari, T.; Oh, K.; Im, S. Electric and Photovoltaic Behavior of a Few-Layer α-MoTe$_2$/MoS$_2$ Dichalcogenide Heterojunction. *Adv. Mater.* **2016**, *28*, 3216–3222. [CrossRef]

11. Rigosi, A.F.; Hill, H.M.; Li, Y.; Chernikov, A.; Heinz, T.F. Probing Interlayer Interactions in Transition Metal Dichalcogenide Heterostructures by Optical Spectroscopy: MoS$_2$/WS$_2$ and MoSe$_2$/WSe$_2$. *Nano Lett.* **2015**, *15*, 5033–5038. [CrossRef]

12. Vajtai, R.; He, Y.; Liu, Z.; Lei, S.; Zhang, X.; Zhou, W.; Ye, G.; Gong, Y.; Lou, J.; Wang, Q.; et al. Two-Step Growth of Two-Dimensional WSe$_2$/MoSe$_2$ Heterostructures. *Nano Lett.* **2015**, *15*, 6135–6141. [CrossRef]

13. Gong, Y.; Lin, J.; Wang, X.; Shi, G.; Lei, S.; Lin, Z.; Zou, X.; Ye, G.; Vajtai, R.; Yakobson, B.I.; et al. Vertical and In-Plane Heterostructures from WS$_2$/MoS$_2$ Monolayers. *Nat. Mater.* **2014**, *13*, 1135–1142. [CrossRef]

14. Zhou, X.; Jiang, J.; Ding, T.; Zhang, J.; Pan, B.; Zuo, J.; Yang, Q. Fast Colloidal Synthesis of Scalable Mo-Rich Hierarchical Ultrathin MoSe$_{2-x}$ nanosheets for High-Performance Hydrogen Evolution. *Nanoscale* **2014**, *6*, 11046–11051. [CrossRef]

15. Sun, D.; Feng, S.; Terrones, M.; Schaak, R.E. Formation and Interlayer Decoupling of Colloidal MoSe$_2$ Nanoflowers. *Chem. Mater.* **2015**, *27*, 3167–3175. [CrossRef]

16. Wu, W.; Zhang, Q.; Zhou, X.; Li, L.; Su, J.; Wang, F.; Zhai, T. Self-Powered Photovoltaic Photodetector Established on Lateral Monolayer MoS$_2$-WS$_2$ Heterostructures. *Nano Energy* **2018**, *51*, 45–53. [CrossRef]

17. Kim, J.E.; Kang, W.T.; Tu Vu, V.; Kim, Y.R.; Shin, Y.S.; Lee, I.; Won, U.Y.; Lee, B.H.; Kim, K.; Phan, T.L.; et al. Ideal PN Photodiode Using Doping Controlled WSe$_2$-MoSe$_2$ Lateral Heterostructure. *J. Mater. Chem. C* **2021**, *9*, 3504–3512. [CrossRef]

18. Lee, C.H.; Lee, G.H.; Van Der Zande, A.M.; Chen, W.; Li, Y.; Han, M.; Cui, X.; Arefe, G.; Nuckolls, C.; Heinz, T.F.; et al. Atomically Thin P-n Junctions with van Der Waals Heterointerfaces. *Nat. Nanotechnol.* **2014**, *9*, 676–681. [CrossRef]

19. Guo, W.; Chen, Y.; Wang, L.; Xu, J.; Zeng, D.; Peng, D.L. Colloidal Synthesis of MoSe$_2$ Nanonetworks and Nanoflowers with Efficient Electrocatalytic Hydrogen-Evolution Activity. *Electrochim. Acta* **2017**, *231*, 69–76. [CrossRef]

20. Liu, Z.; Zhao, H.; Li, N.; Zhang, Y.; Zhang, X.; Du, Y. Assembled 3D Electrocatalysts for Efficient Hydrogen Evolution: WSe$_2$ layers Anchored on Graphene Sheets. *Inorg. Chem. Front.* **2016**, *3*, 313–319. [CrossRef]

21. Abdallah, W.A.; Nelson, A.E. Characterization of MoSe$_2$ (0001) and Ion-Sputtered MoSe$_2$ by XPS. *J. Mater. Sci.* **2005**, *40*, 2679–2681. [CrossRef]

22. Boscher, N.D.; Carmalt, C.J.; Parkin, I.P. Atmospheric Pressure Chemical Vapor Deposition of WSe$_2$ Thin Films on Glass—Highly Hydrophobic Sticky Surfaces. *J. Mater. Chem.* **2006**, *16*, 122–127. [CrossRef]

23. Ambrosi, A.; Sofer, Z.; Pumera, M. 2H → 1T Phase Transition and Hydrogen Evolution Activity of MoS$_2$, MoSe$_2$, WS$_2$ and WSe$_2$ Strongly Depends on the MX2 composition. *Chem. Commun.* **2015**, *51*, 8450–8453. [CrossRef]

24. Liu, X.Y. Heterogeneous nucleation or homogeneous nucleation? *J. Chem. Phys.* **2000**, *112*, 9949–9955. [CrossRef]

25. Viksman, G.S.; Gardienko, S.P.; Klochkov, L.A.; Yanaki, A.A. Dissociation of molybdenum and tungsten selenides. *Sov. Powder Met. Met. Ceram.* **1986**, *25*, 64–66. [CrossRef]

26. Gradečak, S.; Garaj, S.; Bogaert, K.; Titow, D.; Liu, S.; Chesin, J. Diffusion-Mediated Synthesis of MoS$_2$/WS$_2$ Lateral Heterostructures. *Nano Lett.* **2016**, *16*, 5129–5134. [CrossRef]

27. Zeng, H.; Liu, G.B.; Dai, J.; Yan, Y.; Zhu, B.; He, R.; Xie, L.; Xu, S.; Chen, X.; Yao, W.; et al. Optical Signature of Symmetry Variations and Spin-Valley Coupling in Atomically Thin Tungsten Dichalcogenides. *Sci. Rep.* **2013**, *3*, 4908–4916. [CrossRef]

28. Zhang, M.; Wu, J.; Zhu, Y.; Dumcenco, D.O.; Hong, J.; Mao, N.; Deng, S.; Chen, Y.; Yang, Y.; Jin, C.; et al. Two-Dimensional Molybdenum Tungsten Diselenide Alloys: Photoluminescence, Raman Scattering, and Electrical Transport. *ACS Nano* **2014**, *8*, 7130–7137. [CrossRef]

29. Lei, Z.; Xu, S.; Wu, P. Ultra-Thin and Porous MoSe$_2$ nanosheets: Facile Preparation and Enhanced Electrocatalytic Activity towards the Hydrogen Evolution Reaction. *Phys. Chem. Chem. Phys.* **2016**, *18*, 70–74. [CrossRef]

30. Cui, Y. Synthesis of MoS$_2$ and MoSe$_2$ Films with Vertically Aligned Layers. *Nano Lett.* **2013**, *13*, 1341–1347. [CrossRef]

31. Gong, Q.; Cheng, L.; Liu, C.; Zhang, M.; Feng, Q.; Ye, H.; Zeng, M.; Xie, L.; Liu, Z.; Li, Y. Ultrathin MoS$_{2(1-x)}$Se$_{2x}$ Alloy Nanoflakes for Electrocatalytic Hydrogen Evolution Reaction. *ACS Catal.* **2015**, *5*, 2213–2219. [CrossRef]